European Journal of Mechanics B/Fluids 30 (2011) 137–146

Contents lists available at ScienceDirect

European Journal of Mechanics B/Fluids

journal homepage: www.elsevier.com/locate/ejmflu

The localized Zakharov equation: Derivation and validation

O. Gramstad [a,*], Y. Agnon [b], M. Stiassnie [b]

[a] Department of Mathematics, University of Oslo, P.O. Box 1053 Blindern, NO-0316 Oslo, Norway

[b] Faculty of Civil and Environmental Engineering, Technion IIT, Haifa 32000, Israel

ARTICLE INFO

Article history:
Received 12 January 2010
Received in revised form
7 October 2010
Accepted 13 October 2010
Available online 18 November 2010

Keywords:
Water-waves
Nonlinear interaction
Phase-resolving model

ABSTRACT

In Zakharov's equation, the spectral function represents the entire horizontal plane. In practical applications, one often has to use a finite number of Fourier modes that are determined for limited regions of the horizontal plane, but vary from region to region.

To overcome this shortcoming, we utilize a discrete windowed Fourier transform to obtain a new localized Zakharov equation (LZE), which can handle spatial variations in a more transparent way. The LZE is successfully validated by comparing different aspects of its performance with results from the Zakharov equation and a modified nonlinear Schrödinger equation.

1. Introduction

Zakharov's equation [1] is the main existing model to study the weakly nonlinear evolution of sea states with a broad band of wavelengths. Zakharov's equation is deterministic, i.e. no stochastic assumptions were made in the course of its derivation. However, it is also a very convenient starting point for the derivation of Hasselmann's stochastic model [2].

The Zakharov equation is formulated in terms of a generalized amplitude spectrum $\hat{b}(\boldsymbol{k}, t)$, which is determined from the Fourier transform of the surface elevation $\eta(\boldsymbol{x}, t)$ and the Fourier transform of the velocity potential at the free surface $\psi(\boldsymbol{x}, t)$ by

$$\hat{b}(\boldsymbol{k}, t) = \frac{1}{2\pi} \int \left[\left(\frac{g}{2\omega(\boldsymbol{k})} \right)^{1/2} \eta(\boldsymbol{x}, t) + \mathrm{i} \left(\frac{\omega(\boldsymbol{k})}{2g} \right)^{1/2} \psi(\boldsymbol{x}, t) \right] \mathrm{e}^{-\mathrm{i}\boldsymbol{k}\cdot\boldsymbol{x}} \, \mathrm{d}\boldsymbol{x}. \tag{1}$$

Here, $\cdot$ denotes a scalar product; $\boldsymbol{k} = (k_x, k_y)$ is the wavenumber vector; $\boldsymbol{x} = (x, y)$ are the horizontal space coordinates; t is time; g is gravity; and ω is the angular frequency in water of constant depth h given by the dispersion relation $\omega^2 = g|\boldsymbol{k}| \tanh(|\boldsymbol{k}|h)$. Zakharov has shown that the temporal evolution of $\hat{b}(\boldsymbol{k}, t)$ is governed by

$$\mathrm{i}\frac{\partial \hat{b}}{\partial t} - \omega(\boldsymbol{k})\hat{b} = \int T_{0,1,2,3} \hat{b}_1^* \hat{b}_2 \hat{b}_3 \delta_{0+1-2-3} \, \mathrm{d}\boldsymbol{k}_{1,2,3}, \tag{2}$$

which is now called the Zakharov equation. Here, we have used the compact notation, e.g. $\mathrm{d}\boldsymbol{k}_{1,2,3} = \mathrm{d}\boldsymbol{k}_1 \mathrm{d}\boldsymbol{k}_2 \mathrm{d}\boldsymbol{k}_3$ and $\delta_{0+1-2-3} = \delta(\boldsymbol{k} + \boldsymbol{k}_1 - \boldsymbol{k}_2 - \boldsymbol{k}_3)$. The kernel $T_{0,1,2,3} = T(\boldsymbol{k}, \boldsymbol{k}_1, \boldsymbol{k}_2, \boldsymbol{k}_3)$ can be found, for example, in [3], or in an alternative form with modifications necessary for the Zakharov equation to be Hamiltonian [4]. Early numerical simulations of (2) can be found in [5], and more recent references are given by [6]. Note that, strictly speaking, (1) also includes bound modes in addition to the leading-order free modes, whereas (2) is for the free modes only. Details about obtaining the bound modes once the free modes are known can be found in [3].

The inverse of (1) is

$$\eta = \frac{1}{2\pi} \int \left(\frac{\omega}{2g} \right)^{1/2} \left(\hat{b} \mathrm{e}^{\mathrm{i}\boldsymbol{k}\cdot\boldsymbol{x}} + \text{c.c.} \right) \mathrm{d}\boldsymbol{k}, \tag{3a}$$

$$\psi = \frac{-\mathrm{i}}{2\pi} \int \left(\frac{g}{2\omega} \right)^{1/2} \left(\hat{b} \mathrm{e}^{\mathrm{i}\boldsymbol{k}\cdot\boldsymbol{x}} - \text{c.c.} \right) \mathrm{d}\boldsymbol{k}. \tag{3b}$$

The main goal of the current paper is to tackle the following challenge. In the derivation of Zakharov's equation (2), the Fourier transform (1) is applied over the entire horizontal plane, resulting in $\hat{b}(\boldsymbol{k}, t)$—a 'global' amplitude spectrum. In practice, however, i.e. in field or laboratory applications, the Fourier transform is applied only to a limited region of the horizontal plane, resulting in a 'local' amplitude spectrum which varies from region to region.

In Section 2 of this paper, we develop a localized discrete Zakharov equation (LZE), tailored to overcome the above-mentioned

* Corresponding author.
E-mail addresses: oding@math.uio.no (O. Gramstad), agnon@tx.technion.ac.il (Y. Agnon), miky@tx.technion.ac.il (M. Stiassnie).

0997-7546/$ – see front matter © 2010 Elsevier Masson SAS. All rights reserved.
doi:10.1016/j.euromechflu.2010.10.004

difficulty. To capture the local nature of the wave field we use a windowed Fourier transform, so that (1) is replaced by the local amplitude functions

$$b_{m,n}(\boldsymbol{x},t) = \frac{1}{2\pi}\int\left[\left(\frac{g}{2\omega_{m,n}}\right)^{1/2}\eta(\boldsymbol{x}_1,t) + \mathrm{i}\left(\frac{\omega_{m,n}}{2g}\right)^{1/2}\psi(\boldsymbol{x}_1,t)\right]G(\boldsymbol{x}-\boldsymbol{x}_1)\mathrm{e}^{-\mathrm{i}\boldsymbol{k}_{m,n}\cdot\boldsymbol{x}_1}\,\mathrm{d}\boldsymbol{x}_1, \quad (4)$$

where $G(\boldsymbol{x})$ is the window function, $\omega_{m,n}^2 = g|\boldsymbol{k}_{m,n}|\tanh(|\boldsymbol{k}_{m,n}|h)$ and $\boldsymbol{k}_{m,n} = (m\Delta_x, n\Delta_y)$. The inverse of (4) turns out to be

$$\eta(\boldsymbol{x},t) = \sum_{m,n}\left(\frac{\omega_{m,n}}{2g}\right)^{1/2}\left(b_{m,n}(\boldsymbol{x},t)\mathrm{e}^{\mathrm{i}\boldsymbol{k}_{m,n}\cdot\boldsymbol{x}} + \text{c.c.}\right), \quad (5a)$$

$$\psi(\boldsymbol{x},t) = -\mathrm{i}\sum_{m,n}\left(\frac{g}{2\omega_{m,n}}\right)^{1/2}\left(b_{m,n}(\boldsymbol{x},t)\mathrm{e}^{\mathrm{i}\boldsymbol{k}_{m,n}\cdot\boldsymbol{x}} - \text{c.c.}\right), \quad (5b)$$

which are Fourier series, comparable to the inverse Fourier transform of (3).

The governing equation for the local amplitude functions is the new LZE

$$\begin{aligned}&\mathrm{i}\frac{\partial b_{m,n}}{\partial t} - \omega_{m,n}b_{m,n} + \mathrm{i}\boldsymbol{c}_{g\,m,n}\cdot\nabla b_{m,n} \\ &\quad + \frac{D_{m,n}^{(xx)}}{2}\frac{\partial^2 b_{m,n}}{\partial x^2} + D_{m,n}^{(xy)}\frac{\partial^2 b_{m,n}}{\partial x\partial y} + \frac{D_{m,n}^{(yy)}}{2}\frac{\partial^2 b_{m,n}}{\partial y^2} \\ &\quad = 2\pi\sum_{m_1,n_1}\sum_{m_2,n_2}\sum_{m_3,n_3}T(\boldsymbol{k}_{m_3,n_3}+\boldsymbol{k}_{m_2,n_2} \\ &\qquad - \boldsymbol{k}_{m_1,n_1},\boldsymbol{k}_{m_1,n_1},\boldsymbol{k}_{m_2,n_2},\boldsymbol{k}_{m_3,n_3}) \\ &\qquad \times\int b_{m_1,n_1}^*(\boldsymbol{x}_1)b_{m_2,n_2}(\boldsymbol{x}_1)b_{m_3,n_3}(\boldsymbol{x}_1) \\ &\qquad \times\mathrm{e}^{\mathrm{i}(\boldsymbol{k}_{m_3,n_3}+\boldsymbol{k}_{m_2,n_2}-\boldsymbol{k}_{m_1,n_1}-\boldsymbol{k}_{m,n})\cdot\boldsymbol{x}_1}G(\boldsymbol{x}-\boldsymbol{x}_1)\,\mathrm{d}\boldsymbol{x}_1. \end{aligned} \quad (6)$$

The local amplitude functions $b_{m,n}(\boldsymbol{x},t)$ are related to the generalized amplitude spectrum $\hat{b}(\boldsymbol{k},t)$ by

$$b_{m,n}(\boldsymbol{x},t) = \frac{1}{2\pi}\int\hat{b}(\boldsymbol{k},t)g(\boldsymbol{k}-\boldsymbol{k}_{m,n})\mathrm{e}^{\mathrm{i}(\boldsymbol{k}-\boldsymbol{k}_{m,n})\cdot\boldsymbol{x}}\,\mathrm{d}\boldsymbol{k}, \quad (7)$$

where $g(\boldsymbol{k})$ and $G(\boldsymbol{x})$ are a Fourier transform pair

$$g(\boldsymbol{k}) = \frac{1}{2\pi}\int G(\boldsymbol{x})\mathrm{e}^{-\mathrm{i}\boldsymbol{k}\cdot\boldsymbol{x}}\,\mathrm{d}\boldsymbol{x}, \qquad G(\boldsymbol{x}) = \frac{1}{2\pi}\int g(\boldsymbol{k})\mathrm{e}^{\mathrm{i}\boldsymbol{k}\cdot\boldsymbol{x}}\,\mathrm{d}\boldsymbol{k}, \quad (8)$$

and where $g(\boldsymbol{k})$ must satisfy the identity

$$\sum_{m,n}g(\boldsymbol{k}-\boldsymbol{k}_{m,n}) = 1 \quad (9)$$

for any $\boldsymbol{k}$. Window functions which have the property (9) are presented in Appendix A.

Sections 3 and 4 are devoted to the validation of the LZE (6), by comparing its performance to that of other 'benchmark' models. This, however, can be done only for problems for which we have reliable solvers for the benchmark models. Thus, we have decided to restrict ourselves to problems which are periodic in space, and we use Zakharov's equation itself as the main benchmark. The criteria for validation include comparisons of the free surface, of invariants, and of spectral evolution.

The successful validation process and future possible applications are discussed in Section 5. Details of the reconstruction of the free surface are presented in Appendix B. The relation between the LZE and the DZE (discretized Zakharov equation) derived in [7] is given in Appendix C. In Appendix D, the evolution of a single Stokes wave is analyzed and used to estimate the errors introduced by the approximations in the LZE.

2. Derivation of the localized Zakharov equation

2.1. Windowed Fourier transform

The two-dimensional spatial Fourier transform of a function $f(\boldsymbol{x})$ is defined as

$$\hat{f}(\boldsymbol{k}) = \mathcal{F}\{f(\boldsymbol{x})\} = \frac{1}{2\pi}\int f(\boldsymbol{x})\mathrm{e}^{-\mathrm{i}\boldsymbol{k}\cdot\boldsymbol{x}}\,\mathrm{d}\boldsymbol{x}, \quad (10)$$

with the inverse transform in the form

$$f(\boldsymbol{x}) = \mathcal{F}^{-1}\{\hat{f}(\boldsymbol{k})\} = \frac{1}{2\pi}\int\hat{f}(\boldsymbol{k})\mathrm{e}^{\mathrm{i}\boldsymbol{k}\cdot\boldsymbol{x}}\,\mathrm{d}\boldsymbol{k}. \quad (11)$$

Similarly, one can define a windowed Fourier transform by

$$f_w(\boldsymbol{x},\boldsymbol{k}_0) = \frac{1}{2\pi}\int\hat{f}(\boldsymbol{k})g(\boldsymbol{k}-\boldsymbol{k}_0)\mathrm{e}^{\mathrm{i}\boldsymbol{k}\cdot\boldsymbol{x}}\,\mathrm{d}\boldsymbol{k}, \quad (12)$$

where $g(\boldsymbol{k})$ is a window function that is nonzero only in the vicinity of $\boldsymbol{k} = 0$. Assuming that the window function is normalized so that

$$\int g(\boldsymbol{k}_0)\,\mathrm{d}\boldsymbol{k}_0 = \int g(\boldsymbol{k}-\boldsymbol{k}_0)\,\mathrm{d}\boldsymbol{k}_0 = 1 \quad (13)$$

for any $\boldsymbol{k}$, integration of (12) over $\boldsymbol{k}_0$ gives

$$\begin{aligned} f(\boldsymbol{x}) &= \int f_w(\boldsymbol{x},\boldsymbol{k}_0)\,\mathrm{d}\boldsymbol{k}_0, \\ \hat{f}(\boldsymbol{k}) &= \frac{1}{2\pi}\iint f_w(\boldsymbol{x},\boldsymbol{k}_0)\mathrm{d}\boldsymbol{k}_0\mathrm{e}^{-\mathrm{i}\boldsymbol{k}\cdot\boldsymbol{x}}\mathrm{d}\boldsymbol{x}. \end{aligned} \quad (14)$$

In the case of discrete window positions, $\boldsymbol{k}_0 = \boldsymbol{k}_{m,n}$, where $m = 1,\ldots,M$, $n = 1,\ldots,N$, the discrete versions of the above results are obtained as

$$f_{m,n}(\boldsymbol{x}) = \frac{1}{2\pi}\int\hat{f}(\boldsymbol{k})g(\boldsymbol{k}-\boldsymbol{k}_{m,n})\mathrm{e}^{\mathrm{i}\boldsymbol{k}\cdot\boldsymbol{x}}\,\mathrm{d}\boldsymbol{k}, \quad (15)$$

and

$$f(\boldsymbol{x}) = \sum_{m,n}f_{m,n}(\boldsymbol{x}), \qquad \hat{f}(\boldsymbol{k}) = \frac{1}{2\pi}\int\sum_{m,n}f_{m,n}(\boldsymbol{x})\mathrm{e}^{-\mathrm{i}\boldsymbol{k}\cdot\boldsymbol{x}}\,\mathrm{d}\boldsymbol{x}, \quad (16)$$

where the discrete version of (13),

$$\sum_{m,n}g(\boldsymbol{k}-\boldsymbol{k}_{m,n}) = 1, \quad (17)$$

is satisfied. In practice, the criterion (17) puts a strong limitation on the choice of the function g, since the sum (17) must generally be expected to depend on $\boldsymbol{k}$. Some window functions that satisfy (17) are presented in Appendix A.

The grid in the wavenumber space can be chosen to be irregular. This choice may be advantageous under certain circumstances. The present work is formulated, for simplicity, in terms of a regular grid.

2.2. The localized Zakharov equation

The starting point of the derivation of the LZE is Zakharov's equation (2), which describes the temporal evolution of the free, dominant spectral component $\hat{b}(\boldsymbol{k},t)$ of a weakly nonlinear wave field. Based on the previous sections, we define $M \times N$ localized variables

$$b_{m,n}(\boldsymbol{x},t)\mathrm{e}^{\mathrm{i}\boldsymbol{k}_{m,n}\cdot\boldsymbol{x}}, \quad m = 1,\ldots,M,\ n = 1,\ldots,N \quad (18)$$

as discrete windowed Fourier transforms of $\hat{b}(\boldsymbol{k},t)$,

$$b_{m,n}(\boldsymbol{x},t) = \frac{1}{2\pi}\int\hat{b}(\boldsymbol{k},t)g(\boldsymbol{k}-\boldsymbol{k}_{m,n})\mathrm{e}^{\mathrm{i}(\boldsymbol{k}-\boldsymbol{k}_{m,n})\cdot\boldsymbol{x}}\,\mathrm{d}\boldsymbol{k}, \quad (19)$$

for the $M \times N$ discrete window positions $\boldsymbol{k}_{m,n}$. One can show from (16) that the original $b(\boldsymbol{x}, t)$ and $\hat{b}(\boldsymbol{k}, t)$ are obtained as

$$\begin{aligned} b(\boldsymbol{x}, t) &= \sum_{m,n} b_{m,n}(\boldsymbol{x}, t) \mathrm{e}^{\mathrm{i}\boldsymbol{k}_{m,n}\cdot\boldsymbol{x}}, \\ \hat{b}(\boldsymbol{k}, t) &= \frac{1}{2\pi} \sum_{m,n} \int b_{m,n}(\boldsymbol{x}, t) \mathrm{e}^{-\mathrm{i}(\boldsymbol{k}-\boldsymbol{k}_{m,n})\cdot\boldsymbol{x}} \,\mathrm{d}\boldsymbol{x}. \end{aligned} \tag{20}$$

Now, multiplying the Zakharov equation (2) by $g(\boldsymbol{k} - \boldsymbol{k}_{m,n})\,\mathrm{e}^{-\mathrm{i}\boldsymbol{k}_{m,n}\cdot\boldsymbol{x}}$ and applying the inverse Fourier transform gives

$$\begin{aligned} &\frac{1}{2\pi} \int \left[\mathrm{i}\frac{\partial \hat{b}}{\partial t} - \omega(\boldsymbol{k})\hat{b} \right] g(\boldsymbol{k} - \boldsymbol{k}_{m,n}) \mathrm{e}^{\mathrm{i}(\boldsymbol{k}-\boldsymbol{k}_{m,n})\cdot\boldsymbol{x}} \,\mathrm{d}\boldsymbol{k} \\ &\quad = \frac{1}{2\pi} \int T_{3+2-1,1,2,3} \hat{b}_1^* \hat{b}_2 \hat{b}_3 g(\boldsymbol{k}_3 + \boldsymbol{k}_2 - \boldsymbol{k}_1 - \boldsymbol{k}_{m,n}) \\ &\qquad \times \mathrm{e}^{\mathrm{i}(\boldsymbol{k}_3+\boldsymbol{k}_2-\boldsymbol{k}_1-\boldsymbol{k}_{m,n})\cdot\boldsymbol{x}} \,\mathrm{d}\boldsymbol{k}_{1,2,3}. \end{aligned} \tag{21}$$

Since $g(\boldsymbol{k} - \boldsymbol{k}_{m,n})$ is localized around $\boldsymbol{k} = \boldsymbol{k}_{m,n}$, one can replace $\omega(\boldsymbol{k})$ on the left-hand side (LHS) with its Taylor expansion

$$\begin{aligned} \omega(\boldsymbol{k}) = \omega_{m,n} &+ \mathbf{c}_{g_{m,n}} \cdot (\boldsymbol{k} - \boldsymbol{k}_{m,n}) + \frac{1}{2} \frac{\partial^2 \omega}{\partial k_x^2}\bigg|_{\boldsymbol{k}=\boldsymbol{k}_{m,n}} (k_x - k_{xm,n})^2 \\ &+ \frac{\partial^2 \omega}{\partial k_x \partial k_y}\bigg|_{\boldsymbol{k}=\boldsymbol{k}_{m,n}} (k_x - k_{xm,n})(k_y - k_{ym,n}) \\ &+ \frac{1}{2} \frac{\partial^2 \omega}{\partial k_y^2}\bigg|_{\boldsymbol{k}=\boldsymbol{k}_{m,n}} (k_y - k_{ym,n})^2, \end{aligned} \tag{22}$$

where $\mathbf{c}_{g_{m,n}} = \mathbf{c}_g(\boldsymbol{k}_{m,n})$ is the group velocity of a wave with wavenumber vector $\boldsymbol{k}_{m,n}$. From (19), it follows that

$$\begin{aligned} \frac{\partial^{p+q} b_{m,n}}{\partial x^p \partial y^q} &= \frac{1}{2\pi} \int [\mathrm{i}(k_x - k_{xm,n})]^p [\mathrm{i}(k_y - k_{ym,n})]^q \\ &\quad \times \hat{b}(\boldsymbol{k}, t) g(\boldsymbol{k} - \boldsymbol{k}_{m,n}) \mathrm{e}^{\mathrm{i}(\boldsymbol{k}-\boldsymbol{k}_{m,n})\cdot\boldsymbol{x}} \,\mathrm{d}\boldsymbol{k}, \end{aligned} \tag{23}$$

which enables us to write the LHS of (21) as

$$\begin{aligned} \mathrm{LHS} = \mathrm{i}\frac{\partial b_{m,n}}{\partial t} &- \omega_{m,n} b_{m,n} + \mathrm{i}\mathbf{c}_{g_{m,n}} \cdot \nabla b_{m,n} + \frac{D_{m,n}^{(xx)}}{2} \frac{\partial^2 b_{m,n}}{\partial x^2} \\ &+ D_{m,n}^{(xy)} \frac{\partial^2 b_{m,n}}{\partial x \partial y} + \frac{D_{m,n}^{(yy)}}{2} \frac{\partial^2 b_{m,n}}{\partial y^2}, \end{aligned} \tag{24}$$

where we have defined

$$\begin{aligned} D_{m,n}^{(xx)} &= \frac{\partial^2 \omega}{\partial k_x^2}\bigg|_{\boldsymbol{k}=\boldsymbol{k}_{m,n}}, \qquad D_{m,n}^{(xy)} = \frac{\partial^2 \omega}{\partial k_x \partial k_y}\bigg|_{\boldsymbol{k}=\boldsymbol{k}_{m,n}}, \\ D_{m,n}^{(yy)} &= \frac{\partial^2 \omega}{\partial k_y^2}\bigg|_{\boldsymbol{k}=\boldsymbol{k}_{m,n}}. \end{aligned} \tag{25}$$

On infinite water depth, $h \to \infty$, the coefficients take the simple forms

$$\begin{aligned} \mathbf{c}_{g_{m,n}} &= \frac{1}{2} \frac{g\boldsymbol{k}_{m,n}}{\omega_{m,n} k_{m,n}}, \qquad D_{m,n}^{(xx)} = -\frac{1}{4} \frac{g(k_{xm,n}^2 - 2k_{ym,n}^2)}{\omega_{m,n} k_{m,n}^3}, \\ D_{m,n}^{(xy)} &= -\frac{3}{4} \frac{g k_{xm,n} k_{ym,n}}{\omega_{m,n} k_{m,n}^3}, \qquad D_{m,n}^{(yy)} = \frac{1}{4} \frac{g(2k_{xm,n}^2 - k_{ym,n}^2)}{\omega_{m,n} k_{m,n}^3}. \end{aligned} \tag{26}$$

By using (20), the right-hand side (RHS) of (21) can be written in the form

$$\begin{aligned} \mathrm{RHS} = \frac{1}{(2\pi)^4} &\int T_{3+2-1,1,2,3} \\ &\times \left[\sum_{m_1,n_1} \int b_{m_1,n_1}^*(\boldsymbol{x}_1) \mathrm{e}^{\mathrm{i}(\boldsymbol{k}_1 - \boldsymbol{k}_{m_1,n_1})\cdot\boldsymbol{x}_1} \,\mathrm{d}\boldsymbol{x}_1 \right] \\ &\times \left[\sum_{m_2,n_2} \int b_{m_2,n_2}(\boldsymbol{x}_2) \mathrm{e}^{-\mathrm{i}(\boldsymbol{k}_2 - \boldsymbol{k}_{m_2,n_2})\cdot\boldsymbol{x}_2} \,\mathrm{d}\boldsymbol{x}_2 \right] \\ &\times \left[\sum_{m_3,n_3} \int b_{m_3,n_3}(\boldsymbol{x}_3) \mathrm{e}^{-\mathrm{i}(\boldsymbol{k}_3 - \boldsymbol{k}_{m_3,n_3})\cdot\boldsymbol{x}_3} \,\mathrm{d}\boldsymbol{x}_3 \right] \\ &\times g(\boldsymbol{k}_3 + \boldsymbol{k}_2 - \boldsymbol{k}_1 - \boldsymbol{k}_{m,n}) \mathrm{e}^{\mathrm{i}(\boldsymbol{k}_3+\boldsymbol{k}_2-\boldsymbol{k}_1-\boldsymbol{k}_{m,n})\cdot\boldsymbol{x}} \,\mathrm{d}\boldsymbol{k}_{1,2,3}. \end{aligned} \tag{27}$$

By using the fact that most of the contribution to $b_{m,n}$ comes from the vicinity of $\boldsymbol{k} = \boldsymbol{k}_{m,n}$, the kernel $T_{3+2-1,1,2,3}$ can be approximated so that

$$\begin{aligned} \mathrm{RHS} = \frac{1}{(2\pi)^4} &\iint \sum_{m_1,n_1} \sum_{m_2,n_2} \sum_{m_3,n_3} T(\boldsymbol{k}_{m_3,n_3} + \boldsymbol{k}_{m_2,n_2} \\ &- \boldsymbol{k}_{m_1,n_1}, \boldsymbol{k}_{m_1,n_1}, \boldsymbol{k}_{m_2,n_2}, \boldsymbol{k}_{m_3,n_3}) \\ &\times b_{m_1,n_1}^*(\boldsymbol{x}_1) b_{m_2,n_2}(\boldsymbol{x}_2) b_{m_3,n_3}(\boldsymbol{x}_3) \mathrm{e}^{-\mathrm{i}\boldsymbol{k}_{m,n}\cdot\boldsymbol{x}} \\ &\times \mathrm{e}^{-\mathrm{i}\boldsymbol{k}_{m_1,n_1}\cdot\boldsymbol{x}_1} \mathrm{e}^{\mathrm{i}\boldsymbol{k}_{m_2,n_2}\cdot\boldsymbol{x}_2} \mathrm{e}^{\mathrm{i}\boldsymbol{k}_{m_3,n_3}\cdot\boldsymbol{x}_3} \\ &\times g(\boldsymbol{k}_3 + \boldsymbol{k}_2 - \boldsymbol{k}_1 - \boldsymbol{k}_{m,n}) \mathrm{e}^{-\mathrm{i}(\boldsymbol{x}-\boldsymbol{x}_1)\cdot\boldsymbol{k}_1} \\ &\times \mathrm{e}^{\mathrm{i}(\boldsymbol{x}-\boldsymbol{x}_2)\cdot\boldsymbol{k}_2} \mathrm{e}^{\mathrm{i}(\boldsymbol{x}-\boldsymbol{x}_3)\cdot\boldsymbol{k}_3} \,\mathrm{d}\boldsymbol{x}_{1,2,3} \mathrm{d}\,\boldsymbol{k}_{1,2,3}. \end{aligned} \tag{28}$$

We now carry out the integration over $\boldsymbol{k}_1$, $\boldsymbol{k}_2$ and $\boldsymbol{k}_3$ using

$$\begin{aligned} &\frac{1}{2\pi} \int g(\boldsymbol{k}_3 + \boldsymbol{k}_2 - \boldsymbol{k}_1 - \boldsymbol{k}_{m,n}) \mathrm{e}^{-\mathrm{i}(\boldsymbol{x}-\boldsymbol{x}_1)\cdot\boldsymbol{k}_1} \,\mathrm{d}\boldsymbol{k}_1 \\ &\quad = \mathrm{e}^{-\mathrm{i}(\boldsymbol{x}-\boldsymbol{x}_1)\cdot(\boldsymbol{k}_3+\boldsymbol{k}_2-\boldsymbol{k}_{m,n})} \frac{1}{2\pi} \int g(\mathbf{u}) \mathrm{e}^{\mathrm{i}(\boldsymbol{x}-\boldsymbol{x}_1)\cdot\mathbf{u}} \,\mathrm{d}\mathbf{u} \\ &\quad = \mathrm{e}^{-\mathrm{i}(\boldsymbol{x}-\boldsymbol{x}_1)\cdot(\boldsymbol{k}_3+\boldsymbol{k}_2-\boldsymbol{k}_{m,n})} G(\boldsymbol{x} - \boldsymbol{x}_1) \end{aligned} \tag{29}$$

and

$$\begin{aligned} &\frac{1}{(2\pi)^2} \int \mathrm{e}^{\mathrm{i}\boldsymbol{k}_2\cdot(\boldsymbol{x}_1-\boldsymbol{x}_2)} \mathrm{e}^{\mathrm{i}\boldsymbol{k}_3\cdot(\boldsymbol{x}_1-\boldsymbol{x}_3)} \,\mathrm{d}\boldsymbol{k}_{2,3} \\ &\quad = (2\pi)^2 \delta(\boldsymbol{x}_2 - \boldsymbol{x}_1) \delta(\boldsymbol{x}_3 - \boldsymbol{x}_1), \end{aligned} \tag{30}$$

where $G(\boldsymbol{x})$ is the inverse Fourier transform of $g(\boldsymbol{k})$, so that (28) becomes

$$\begin{aligned} \mathrm{RHS} &= 2\pi \int \sum_{m_1,n_1} \sum_{m_2,n_2} \sum_{m_3,n_3} T(\boldsymbol{k}_{m_3,n_3} + \boldsymbol{k}_{m_2,n_2} \\ &\quad - \boldsymbol{k}_{m_1,n_1}, \boldsymbol{k}_{m_1,n_1}, \boldsymbol{k}_{m_2,n_2}, \boldsymbol{k}_{m_3,n_3}) \\ &\quad \times b_{m_1,n_1}^*(\boldsymbol{x}_1) b_{m_2,n_2}(\boldsymbol{x}_2) b_{m_3,n_3}(\boldsymbol{x}_3) \\ &\quad \times \mathrm{e}^{-\mathrm{i}\boldsymbol{k}_{m,n}\cdot\boldsymbol{x}_1} \mathrm{e}^{-\mathrm{i}\boldsymbol{k}_{m_1,n_1}\cdot\boldsymbol{x}_1} \mathrm{e}^{\mathrm{i}\boldsymbol{k}_{m_2,n_2}\cdot\boldsymbol{x}_2} \mathrm{e}^{\mathrm{i}\boldsymbol{k}_{m_3,n_3}\cdot\boldsymbol{x}_3} \\ &\quad \times G(\boldsymbol{x} - \boldsymbol{x}_1) \delta(\boldsymbol{x}_2 - \boldsymbol{x}_1) \delta(\boldsymbol{x}_3 - \boldsymbol{x}_1) \,\mathrm{d}\boldsymbol{x}_{1,2,3} \\ &= 2\pi \sum_{m_1,n_1} \sum_{m_2,n_2} \sum_{m_3,n_3} T(\boldsymbol{k}_{m_3,n_3} + \boldsymbol{k}_{m_2,n_2} \\ &\quad - \boldsymbol{k}_{m_1,n_1}, \boldsymbol{k}_{m_1,n_1}, \boldsymbol{k}_{m_2,n_2}, \boldsymbol{k}_{m_3,n_3}) \\ &\quad \times \int b_{m_1,n_1}^*(\boldsymbol{x}_1) b_{m_2,n_2}(\boldsymbol{x}_1) b_{m_3,n_3}(\boldsymbol{x}_1) \\ &\quad \times \mathrm{e}^{\mathrm{i}(\boldsymbol{k}_{m_3,n_3} + \boldsymbol{k}_{m_2,n_2} - \boldsymbol{k}_{m_1,n_1} - \boldsymbol{k}_{m,n})\cdot\boldsymbol{x}_1} G(\boldsymbol{x} - \boldsymbol{x}_1) \,\mathrm{d}\boldsymbol{x}_1. \end{aligned} \tag{31}$$

Combining the LHS and RHS, as well as introducing $b_{m,n} = B_{m,n} \mathrm{e}^{-\mathrm{i}\omega_{m,n}t}$, gives the final result:

$$\begin{aligned}
&\mathrm{i}\left(\frac{\partial B_{m,n}}{\partial t} + \mathbf{c}_{g_{m,n}} \cdot \nabla B_{m,n}\right) + \frac{D^{(xx)}_{m,n}}{2}\frac{\partial^2 B_{m,n}}{\partial x^2} \\
&\quad + D^{(xy)}_{m,n}\frac{\partial^2 B_{m,n}}{\partial x \partial y} + \frac{D^{(yy)}_{m,n}}{2}\frac{\partial^2 B_{m,n}}{\partial y^2} \\
&\quad = \sum_{m_1,n_1}\sum_{m_2,n_2}\sum_{m_3,n_3} T(\boldsymbol{k}_{m_3,n_3} + \boldsymbol{k}_{m_2,n_2} \\
&\qquad - \boldsymbol{k}_{m_1,n_1}, \boldsymbol{k}_{m_1,n_1}, \boldsymbol{k}_{m_2,n_2}, \boldsymbol{k}_{m_3,n_3}) \\
&\qquad \times 2\pi \int B^*_{m_1,n_1}(\boldsymbol{x}_1) B_{m_2,n_2}(\boldsymbol{x}_1) B_{m_3,n_3}(\boldsymbol{x}_1) \\
&\qquad \times \mathrm{e}^{\mathrm{i}\theta} G(\boldsymbol{x} - \boldsymbol{x}_1)\, \mathrm{d}\boldsymbol{x}_1, \qquad (32)
\end{aligned}$$

where $\theta = (\boldsymbol{k}_{m_3,n_3} + \boldsymbol{k}_{m_2,n_2} - \boldsymbol{k}_{m_1,n_1} - \boldsymbol{k}_{m,n}) \cdot \boldsymbol{x}_1 - (\omega_{m_3,n_3} + \omega_{m_2,n_2} - \omega_{m_1,n_1} - \omega_{m,n})t$. An alternative representation of (32) may be obtained by using the convolution theorem

$$\int f(\boldsymbol{x}_1) h(\boldsymbol{x} - \boldsymbol{x}_1)\, \mathrm{d}\boldsymbol{x}_1 = 2\pi \mathcal{F}^{-1}\left\{\mathcal{F}\{f\}\mathcal{F}\{h\}\right\}, \qquad (33)$$

which gives

$$\begin{aligned}
&\mathrm{i}\left(\frac{\partial B_{m,n}}{\partial t} + \mathbf{c}_{g_{m,n}} \cdot \nabla B_{m,n}\right) + \frac{D^{(xx)}_{m,n}}{2}\frac{\partial^2 B_{m,n}}{\partial x^2} \\
&\quad + D^{(xy)}_{m,n}\frac{\partial^2 B_{m,n}}{\partial x \partial y} + \frac{D^{(yy)}_{m,n}}{2}\frac{\partial^2 B_{m,n}}{\partial y^2} \\
&\quad = (2\pi)^2 \sum_{m_1,n_1}\sum_{m_2,n_2}\sum_{m_3,n_3} T(\boldsymbol{k}_{m_3,n_3} + \boldsymbol{k}_{m_2,n_2} \\
&\qquad - \boldsymbol{k}_{m_1,n_1}, \boldsymbol{k}_{m_1,n_1}, \boldsymbol{k}_{m_2,n_2}, \boldsymbol{k}_{m_3,n_3}) \\
&\qquad \times \mathcal{F}^{-1}\left\{\mathcal{F}\left\{B^*_{m_1,n_1}(\boldsymbol{x}) B_{m_2,n_2}(\boldsymbol{x}) B_{m_3,n_3}(\boldsymbol{x}) \mathrm{e}^{\mathrm{i}\theta}\right\} \mathcal{F}\left\{G(\boldsymbol{x})\right\}\right\}. \qquad (34)
\end{aligned}$$

For some applications it may be more convenient to write the equation in wavenumber space, i.e.

$$\begin{aligned}
\frac{\partial \hat{B}_{m,n}}{\partial t} &= -\mathrm{i}\left[\mathbf{c}_{g_{m,n}} \cdot \boldsymbol{k}_{m,n} + k_x^2 \frac{D^{(xx)}_{m,n}}{2} + k_x k_y D^{(xy)}_{m,n} + k_y^2 \frac{D^{(yy)}_{m,n}}{2}\right] \hat{B}_{m,n} \\
&\quad - \mathrm{i}(2\pi)^2 \sum_{m_1,n_1}\sum_{m_2,n_2}\sum_{m_3,n_3} T(\boldsymbol{k}_{m_3,n_3} + \boldsymbol{k}_{m_2,n_2} \\
&\quad - \boldsymbol{k}_{m_1,n_1}, \boldsymbol{k}_{m_1,n_1}, \boldsymbol{k}_{m_2,n_2}, \boldsymbol{k}_{m_3,n_3}) \\
&\quad \times \mathcal{F}\left\{B^*_{m_1,n_1}(\boldsymbol{x}) B_{m_2,n_2}(\boldsymbol{x}) B_{m_3,n_3}(\boldsymbol{x}) \mathrm{e}^{\mathrm{i}\theta}\right\} g(\boldsymbol{k}). \qquad (35)
\end{aligned}$$

Moreover, one may also include exact linear dispersion in (35) by replacing the Taylor expansion in (22) with the exact function. Thus

$$\begin{aligned}
\frac{\partial \hat{B}_{m,n}}{\partial t} &= -\mathrm{i}\left[\omega(\boldsymbol{k}_{m,n} + \boldsymbol{k}) - \omega(\boldsymbol{k}_{m,n})\right] \hat{B}_{m,n} \\
&\quad - \mathrm{i}(2\pi)^2 \sum_{m_1,n_1}\sum_{m_2,n_2}\sum_{m_3,n_3} T(\boldsymbol{k}_{m_3,n_3} + \boldsymbol{k}_{m_2,n_2} \\
&\quad - \boldsymbol{k}_{m_1,n_1}, \boldsymbol{k}_{m_1,n_1}, \boldsymbol{k}_{m_2,n_2}, \boldsymbol{k}_{m_3,n_3}) \\
&\quad \times \mathcal{F}\left\{B^*_{m_1,n_1}(\boldsymbol{x}) B_{m_2,n_2}(\boldsymbol{x}) B_{m_3,n_3}(\boldsymbol{x}) \mathrm{e}^{\mathrm{i}\theta}\right\} g(\boldsymbol{k}). \qquad (36)
\end{aligned}$$

2.3. Asymptotic considerations

The derivation of the original Zakharov equation (2) is based on the existence of a small dimensionless parameter $\tilde{\epsilon}$ related to the wave steepness, which is based on the total energy and the spectral peak wavenumber. From (2), one can write $\hat{b}(\boldsymbol{k}, t) = \hat{B}(\tilde{\epsilon}^2 t)\mathrm{e}^{-\mathrm{i}\omega(\boldsymbol{k})t}$, since $\hat{b} = O(\tilde{\epsilon})$. In the derivation of the LZE we have introduced an additional small dimensionless parameter $\tilde{\Delta}$, through the definition of the window functions, given in Appendix A, which is the ratio of the window width Δ to the spectral peak wavenumber. Substituting $b_{m,n} = B_{m,n}\mathrm{e}^{-\mathrm{i}\omega_{m,n}t}$ and $\hat{b} = \hat{B}\mathrm{e}^{-\mathrm{i}\omega t}$ into (19) gives

$$\begin{aligned}
B_{m,n}(\boldsymbol{x}, t) &= \frac{1}{2\pi}\int \hat{B}(\boldsymbol{k}, t) g(\boldsymbol{k} - \boldsymbol{k}_{m,n}) \\
&\quad \times \mathrm{e}^{\mathrm{i}[(\boldsymbol{k} - \boldsymbol{k}_{m,n})\cdot\boldsymbol{x} - (\omega - \omega_{m,n})t]}\, \mathrm{d}\boldsymbol{k}. \qquad (37)
\end{aligned}$$

The narrowness of the window functions and the structure of (37) render

$$B_{m,n}(\boldsymbol{x}, t) = B_{m,n}(\tilde{\Delta}(\boldsymbol{x} - \mathbf{c}_{g_{m,n}}t), \tilde{\epsilon}^2 t). \qquad (38)$$

Referring to the various terms in the LZE (32) as advective (the first two on the LHS), dispersive (the last three terms on the LHS) and nonlinear (the RHS), we note the following. (i) The combined advective terms are of order $\tilde{\epsilon}^3$, (ii) each of the dispersive terms, as well as their combination, are of order $\tilde{\epsilon}\tilde{\Delta}^2$, and (iii) the nonlinear term is of order $\tilde{\epsilon}^3$. Thus consistency imposes the restriction: $O(\tilde{\Delta}/\tilde{\epsilon}) \leq 1$. In our following numerical examples, we have taken $O(\tilde{\Delta}/\tilde{\epsilon}) = 1$. It is reassuring to note that the LZE (32) reduces back to the original Zakharov equation for $\hat{B}(\boldsymbol{k}, t)$ when one lets $\Delta \to 0$.

3. Numerical implementation of the localized Zakharov equation

In the following, we present numerical simulations with the LZE, and perform comparisons with other numerical models in order to validate the LZE and its numerical solution. For this purpose, we solve the equation numerically in a periodic one-dimensional domain. This relatively simple numerical method enables us to validate the LZE by comparing it with other well-established models: a modified nonlinear Schrödinger equation and the Zakharov equation (ZE). We anticipate that the solver can be easily extended to two horizontal dimensions and to allow for other types of boundary conditions. This is left for future studies.

3.1. Numerical method

Since we impose periodic boundary conditions, we can make use of the discrete Fourier transform (fft routines) to switch between physical space and wavenumber space. In this case, it is convenient to use the LZE in the forms given in (35) and (36), where the spatial derivatives in (32) are calculated using Fourier transforms.

The integration in time is performed using a variable time step Runge–Kutta scheme (*ode45* in Matlab). The accuracy of the numerical solution is controlled internally by the solver in agreement with pre-chosen relative and absolute error tolerances. The solver chooses the time step so that the error in the solution at every time step is smaller than the error tolerances.

In order to represent the localized variables $B_{m,n}(\boldsymbol{x})$ numerically, discrete versions of the $\boldsymbol{k}$-plane and $\boldsymbol{x}$-plane are introduced. The part of the wavevector plane described by $k_{x\min} \leq k_x \leq k_{x\max}$ and $k_{y\min} \leq k_y \leq k_{y\max}$ is discretized by an evenly spaced grid with $n_x \times n_y$ grid points. The discrete wavenumber vector is written as

$$\begin{aligned}
\boldsymbol{k}_{p,q} &= \left(k_{x\min} + p\Delta k_x, k_{y\min} + q\Delta k_y\right), \\
&\quad p = 0, \ldots, n_x - 1,\ q = 0, \ldots, n_y - 1, \qquad (39)
\end{aligned}$$

where the spacings between the discretization points are given by

$$\Delta k_x = \frac{k_{x\max} - k_{x\min}}{n_x - 1}, \qquad \Delta k_y = \frac{k_{y\max} - k_{y\min}}{n_y - 1}. \qquad (40)$$

The corresponding discrete $\boldsymbol{x}$-plane becomes

$$\boldsymbol{x}_{p,q} = (p\Delta x, q\Delta y), \quad p = 0, \ldots, n_x - 1,\ q = 0, \ldots, n_y - 1, \qquad (41)$$

where the grid spacings in the $\boldsymbol{x}$ domain are

$$\Delta x = \frac{2\pi}{\Delta k_x n_x}, \qquad \Delta y = \frac{2\pi}{\Delta k_y n_y}. \tag{42}$$

3.2. Initialization of the localized variables

As an initial condition, one needs the $M \times N$ localized variables $B_{m,n}(\boldsymbol{x})$ at $t = 0$. These are easily obtained from (19) if one knows the amplitude spectrum $\hat{b}(\boldsymbol{k}, t = 0)$. The variable $\hat{b}(\boldsymbol{k}, t = 0)$ is typically chosen so that it corresponds to a specific surface displacement or a specific wave spectrum.

Further, one needs to specify the window function $g(\boldsymbol{k})$. Some possible choices of window functions are discussed in Appendix A.

One also has to choose the centers $\boldsymbol{k}_{m,n}$ of the $M \times N$ localized variables (bins) used to represent the full spectral amplitude $\hat{b}(\boldsymbol{k})$. It turns out to be convenient to choose the bin positions $\boldsymbol{k}_{m,n}$ so that they coincide with points in the finer grid $\boldsymbol{k}_{p,q}$. This requires that

$$\Delta_x = l_x \Delta k_x, \qquad \Delta_y = l_y \Delta k_y, \tag{43}$$

where Δ_x and Δ_y are the spacings between the bin centers $\boldsymbol{k}_{m,n}$ in the k_x and k_y directions, respectively, and where l_x and l_y are integers.

In general, one would expect the approximations applied in the derivation of the LZE to be increasingly accurate with an increasing number of localized variables (larger M and N). The effect of the number of localized variables on the accuracy is investigated through numerical simulations in Section 4.

3.3. Efficiency of the numerical solver

By far the most computationally demanding part of solving the equation is evaluating the integral on the RHS of (32) at each integration step. Since the integral is located inside the sums, one has to evaluate $O(M^4N^4)$ integrals.

However, the window functions g, which are narrow banded, can be chosen to be nonzero on a compact support, in a way that there is overlap at most with neighboring windows. One can show that this will greatly limit the number of interactions across windows, to sets for which $m + m_1 \approx m_2 + m_3$ and $n + n_1 \approx n_2 + n_3$. In the case that the window functions are non-overlapping, i.e. $g(\boldsymbol{k}) = 0$ for $|k_x| > \Delta_x/2$, $|k_y| > \Delta_y/2$, it can be shown that it is sufficient to evaluate the triple sum on the RHS for combinations where $|m_3 + m_2 - m_1 - m| \in \{0, 1\}$ and $|n_3 + n_2 - n_1 - n| \in \{0, 1\}$. Correspondingly, for cases where a window function only overlaps with its closest neighbors, i.e. $g(\boldsymbol{k}) = 0$ for $|k_x| > \Delta_x$, $|k_y| > \Delta_y$, it is sufficient to account for $|m_3 + m_2 - m_1 - m| \in \{0, 1, 2, 3\}$ and $|n_3 + n_2 - n_1 - n| \in \{0, 1, 2, 3\}$. In these two cases it can be shown that the number of combinations reduces to approximately $2^d M^3 N^3$ and $(14/3)^d M^3 N^3$, respectively. For two horizontal dimensions, set $d = 2$. For one horizontal dimension, set $d = N = 1$. In Appendix A, several examples of window functions are discussed.

4. Validation

In order to validate the LZE, and to test the numerical solver, a number of validation tests have been performed. For this purpose, two different types of initial spectrum have been employed: a narrow Gaussian spectrum and a broad Pierson–Moskowitz (PM) spectrum. These two spectra have the forms

$$S_G(k) = \frac{\epsilon^2}{2k_c^2\sigma\sqrt{2\pi}} \exp\left(-\frac{(k-k_c)^2}{2k_c^2\sigma^2}\right), \tag{44a}$$

$$S_{PM}(k) = \frac{\alpha}{k^3} \exp\left(-\frac{5}{4}(k/k_c)^{-2}\right). \tag{44b}$$

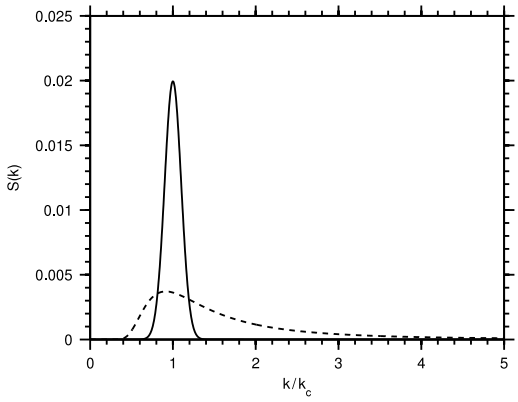

Fig. 1. The two types of initial spectra: Gaussian spectrum (solid line), PM spectrum (dashed line).

Here, ϵ is the steepness of the waves, defined by $\epsilon = k_c\sqrt{2\overline{\eta^2}}$, where the overbar denotes averaging. For both spectra, the total energy was chosen so that the wave steepness $\epsilon = 0.1$. Thus, α in (44b) was chosen in order to give $\epsilon = 0.1$. The width parameter σ in the Gaussian spectrum (44a) was set to 0.1. The phases were chosen randomly on the interval $[0, 2\pi)$. The two spectra are shown in Fig. 1.

To represent the narrow Gaussian spectrum, the part of the k-axis $k \in (0, 2k_c)$ was discretized using $n_x = 122$ grid points. For the broader PM spectrum, the k-axis was resolved up to $k = 4k_c$ using $n_x = 242$ points. One should note that, since the basic unknown of the LZE corresponds to the free-wave part of the wave field only, the grid does not need to represent the higher harmonic bound modes. Therefore, a smaller part of the k-axis may be used compared to other methods which have the full wave field (both free and bound modes) as their unknowns.

In the following, these two initial spectra are used in various test cases in order to validate the LZE and to check its performance compared to other models. In order to investigate the effect of the number of localized variables M, different values of M are employed.

The results presented in the following have been obtained using a cos-type window function (see Appendix A for details). Some preliminary testing showed that overall the cos window showed the best performance, taking accuracy and efficiency into account.

4.1. Comparison with other models

In the derivation of the LZE, both the linear and nonlinear parts of the original Zakharov equation are approximated by using the narrowness of the localized variables. These two approximations, appearing on the LHS and RHS of (32), respectively, may be tested separately in order to identify the error introduced by each approximation. This is performed by comparing the evolution of a specific initial condition using both the LZE and the ZE. For information about the numerical implementation of the ZE, see e.g. [8]. In addition, comparison with a higher-order nonlinear Schrödinger model is also presented. The nonlinear Schrödinger model employed in the following is the Dysthe equation [9], with additional exact linear dispersion (EMNLS equation) [10].

We note that although exact linear dispersion could be included in the LZE when using the present numerical model, it is still of interest to consider the approximation of the linear part. For example, in some applications, one may need to employ a different numerical approach (e.g. nonperiodic boundary conditions), where the form (32) of the LZE must be employed. Therefore, it is useful to check the effect of truncated linear dispersion in addition to the approximation introduced in the nonlinear part of the equation.

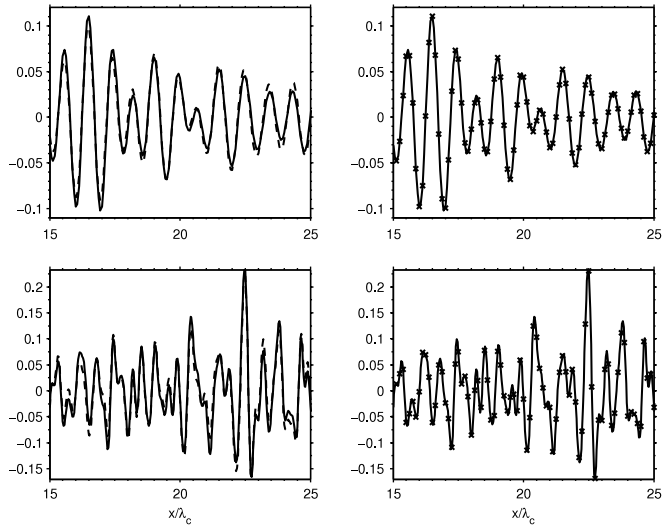

Fig. 2. Surface elevation at $t = 1000T_p$ obtained using the linear LZE without exact linear dispersion and the linear ZE. Upper part: Gaussian initial spectrum; left: linear LZE with $M = 11$ (dashed line) compared to linear ZE (solid line), right: linear LZE with $M = 21$ ($\times$) compared to linear ZE (solid line). Lower part: PM initial spectrum; left: linear LZE with $M = 21$ (dashed line) compared to linear ZE (solid line), right: linear LZE with $M = 41$ ($\times$) compared to linear ZE (solid line).

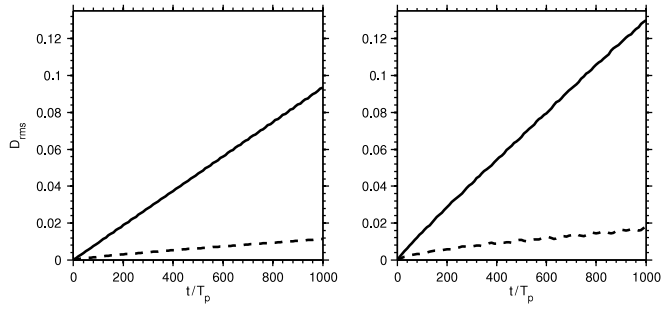

Fig. 3. The time evolution of D_{rms} defined by (45) calculated from the difference between the result from the linear ZE and the linear LZE. Left: Gaussian initial spectrum (solid line, $M = 11$; dashed line, $M = 21$). Right: PM initial spectrum (solid line, $M = 21$; dashed line, $M = 41$).

In order to test the linear approximation in the LZE, we turn off the nonlinear terms in both the ZE and in the LZE, i.e. exclude the RHSs of (2) and (32), and consider the evolution of the same initial condition using the two models. Fig. 2 shows the surface elevation obtained from simulation with the linear LZE (using the two different values of M) compared to the corresponding result from the linear ZE after an evolution time of $1000T_p$, T_p being the peak wave period. The upper part of Fig. 2 shows the result from the Gaussian initial spectrum, while the lower part corresponds to the PM spectrum. In Fig. 3, a normalized rms value, D_{rms}, of the difference between the obtained results is shown. We define D_{rms} as

$$D_{\mathrm{rms}} = \frac{\sqrt{\overline{(\eta_1 - \eta_2)^2}}}{D_0}, \tag{45}$$

where the overbar represents averaging over $\boldsymbol{x}$, and where D_0 is the expected value of the numerator in (45) if η_1 and η_2 are uncorrelated so that $\overline{\eta_1\eta_2} = 0$. If η_1 and η_2 have the same steepness ϵ, one can show that $D_0 = \epsilon/k_c$. Hence, $D_{\mathrm{rms}} = 0$ means that $\eta_1 = \eta_2$, while $D_{\mathrm{rms}} \approx 1$ means that η_1 and η_2 are uncorrelated. The expression for $\eta(\boldsymbol{x}, t)$ in terms of $B_{m,n}(\boldsymbol{x}, t)$ is given in Appendix B.

From Figs. 2 and 3, we note that the differences between the results obtained using exact linear dispersion (linear ZE) and the truncated linear dispersion (linear LZE) are fairly minor. Even

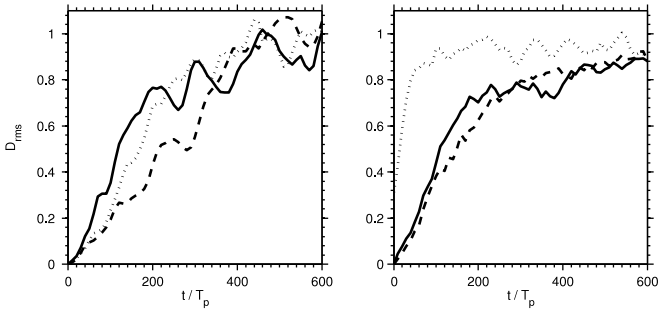

Fig. 4. The time evolution of D_{rms} calculated from the difference between the result from the ZE and the LZE. The difference between the ZE and the EMNLS is shown by the dotted line. Left: Gaussian initial spectrum (solid line, $M = 11$; dashed line, $M = 21$). Right: PM initial spectrum (solid line, $M = 21$; dashed line, $M = 41$).

after $t = 1000T_p$ the results are very similar. The approximation is better for the largest value of M. This is expected, since the accuracy of the Taylor expansion (22) is best close to the bin centers $\boldsymbol{k}_{m,n}$.

We now perform a similar testing of the full LZE, including the nonlinear term in (32). In addition to the comparison with the ZE, we also perform a comparison with the nonlinear Schrödinger model (the EMNLS equation). Fig. 4 shows how the LZE and the EMNLS compare to the full ZE, in terms of the rms value D_{rms}. In both cases, D_{rms}, calculated from the solutions of the LZE, approaches 1 after about 300–400 wave periods. As for the linear case, the results are somewhat better when using a larger number of bins. Based on the evolution of D_{rms}, we note that the LZE performs comparably to the nonlinear Schrödinger model for the narrow Gaussian spectrum. Not surprisingly, the nonlinear Schrödinger model performs rather poorly for the broader PM initial spectrum.

When considering the decorrelation of the solutions shown in Fig. 4, one should recall that in the LZE the interaction coefficients $T_{0,1,2,3}$ are approximated by Taylor expansions around the bin centers. That is, all modes falling within one bin are assigned with the interaction coefficients corresponding to the bin centers. By treating the simple case of a Stokes wave, one can show that D_{rms} is expected to approach 1 on the time scale $t = O(\Delta^{-3}, \epsilon^{-2}\Delta^{-1})$ (see Appendix D for details), where Δ is the width of the window functions and ϵ is the wave steepness. However, as noted in [8], the 'predictability' of the system is in any case limited by the stochastization taking place on $O(10^3)$ wave periods. Hence, the results in Fig. 4 and the analysis in Appendix D indicate that for sufficiently small Δ the approximation errors introduced by the LZE do not significantly limit the time scale for which the LZE can be used to predict a deterministic evolution.

4.2. Invariants

Another check of the accuracy of the numerical solution may be obtained by considering invariants of the equation. We have not succeeded in finding invariants for the new LZE. However, since the LZE is derived starting from the ZE, we consider two of the invariants of the ZE, the wave action and wave momentum, given, respectively, by

$$I = \int |\hat{b}|^2 \,\mathrm{d}\boldsymbol{k}, \qquad \mathbf{J} = \int \boldsymbol{k}|\hat{b}|^2 \,\mathrm{d}\boldsymbol{k}. \tag{46}$$

By using (B.2), one can show that, in terms of the variable in the LZE, $\hat{B}_{m,n}$, (46) can be written as

$$I = \sum_{m_1,n_1}\sum_{m_2,n_2} \int \hat{B}_{m_1,n_1}(\boldsymbol{k} - \boldsymbol{k}_{m_1,n_2})\hat{B}^*_{m_2,n_2}(\boldsymbol{k} - \boldsymbol{k}_{m_2,n_2}) \times \mathrm{e}^{-\mathrm{i}(\omega_{m_1,n_1} - \omega_{m_2,n_2})t} \,\mathrm{d}\boldsymbol{k}, \tag{47a}$$

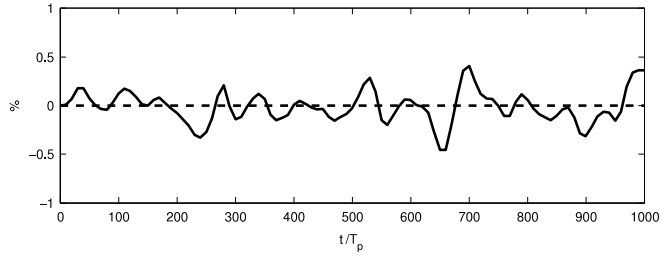

Fig. 5. Relative variation (in per cent) of the wave action for the Gaussian initial spectrum using $M = 41$ bins.

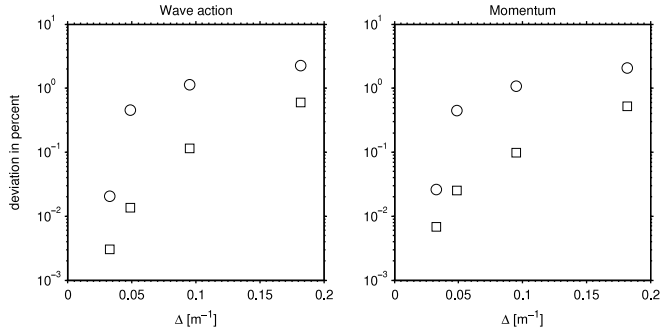

Fig. 6. Maximum (circles) and average (squares) variation over 1000 periods of the invariants (in per cent of initial values) as a function of the bin width Δ used in the numerical simulation.

$$\mathbf{J} = \sum_{m_1,n_1} \sum_{m_2,n_2} \int \boldsymbol{k} \hat{B}_{m_1,n_1}(\boldsymbol{k} - \boldsymbol{k}_{m_1,n_2}) \hat{B}^*_{m_2,n_2}(\boldsymbol{k} - \boldsymbol{k}_{m_2,n_2}) \times \mathrm{e}^{-\mathrm{i}(\omega_{m_1,n_1} - \omega_{m_2,n_2})t}\, \mathrm{d}\boldsymbol{k}. \tag{47b}$$

As an example, the relative deviation of the wave action, in per cent from the initial value, for the case of a Gaussian initial spectrum using $M = 41$ bins is shown in Fig. 5. As indicated by the figure, there is no increasing or decreasing trend for the invariants, but merely fluctuations around the initial value. The magnitude of these fluctuations is found to depend on the number of bins used in the LZE. This is not surprising, since the accuracy of the LZE improves with decreasing bin width Δ. Note that, as $\Delta \to 0$, the LZE reduces to the ZE. The accuracy of the invariants as a function of Δ, obtained using $M = 11, 21, 41$ and 61 bins in the case of Gaussian initial spectrum, is shown in Fig. 6. The circles and squares show the maximum and average variation over 1000 periods of the invariants, respectively.

4.3. Evolution of the wave spectrum

In this section, we use the LZE to investigate the nonlinear evolution of the wave spectrum for our two test cases. By performing 100 realizations of the same initial spectrum, but with different random phases, the wave spectrum can be estimated as an ensemble average of the 100 realizations.

Fig. 7 shows the estimated spectra at three different times ($t = 0$, $t = 100T_p$ and $t = 1000T_p$) obtained using the LZE for two different values of M as well as the ZE. As is clear from the figure, the different models all predict the same features of the wave spectrum.

During the first part of the nonlinear evolution, the narrow Gaussian spectrum broadens and stabilizes in a more broad state; note that the spectrum is more or less identical at $t = 100T_p$ and $t = 1000T_p$. One also sees a small downshift of the spectral peak. These features are all consistent with other numerical experiments [11]. For the PM spectrum much less happens, and the spectrum remains very close to its initial shape throughout the evolution. This is also expected, and is consistent with other results [12].

5. Discussion

A new equation for the nonlinear evolution of water-wave fields has been developed, and has been given the name Localized Zakharov Equation (LZE). The validity of the LZE has been carefully checked by three different tests, all based on comparison with the Zakharov equation, and was found satisfactory. All three tests were applied to a narrow-banded sea as well as a broad-banded sea.

The first test compares individual solutions obtained from numerical simulations with the ZE, the LZE and a nonlinear Schrödinger model. The difference between the individual solutions is represented by D_{rms}—the root mean square normalized deviation of the free surface. We find that the solutions diverge and D_{rms} approaches unity after about 300–400 typical wave periods. This result is consistent with the error introduced by the approximation of the interaction coefficient in the LZE. A simplified example to illustrate this is presented in Appendix D.

We did not succeed in finding invariants for the new LZE. However, in our second test of the LZE, we demonstrate that the wave action and wave momentum only deviate slightly from their initial values throughout the evolution, i.e. over a duration of 1000 peak periods. The magnitude of the deviations decreases significantly with decreasing width of the window functions in the LZE.

In the third test, we have shown that the performance of the LZE cannot be distinguished from that of the Zakharov equation when the evolutions of wave spectra, obtained from ensemble averaging over 100 realizations, are compared. The results for the narrow spectrum are very similar to those of [11], and those for the broad spectrum agree with [12].

We believe that the thorough validation presented herein puts the LZE on firm ground. Note that the earlier attempt to derive a similar model equation is given in [7], where they derived a discretized Zakharov equation (DZE). Their derivation suffered from a scale-separation error, and produced a result of restricted value. The relation between the LZE and the DZE is presented in Appendix C.

The LZE is more cumbersome than the original Zakharov equation. However, it has the potential to handle spatially inhomogeneous problems, in a more physically transparent fashion than its 'mother' equation. In particular, it is suitable for handling future challenges, which fall under the category of 'deterministic sea wave prediction'. Note that the LZE is hybrid in the sense that it resides in both the physical, (x, y), and wavenumber, (k_x, k_y), planes. It is defined on a discrete set of points in the wavenumber plane, and on some part of the continuous physical plane. The hybrid nature of the LZE enables us to introduce a variety of boundary and free-surface features such as wave-makers, absorbing layers and inhomogeneous wind influences. The types of applications of the LZE, ordered by their increasing complexity are (i) a numerical wave flume, (ii) a numerical wave wind tunnel, (iii) a numerical wave basin, and (iv) deterministic short-range sea-wave prediction, to improve autonomous navigation of watercraft.

Acknowledgements

This research was supported by The Israel Science Foundation (Grants 695/04 and 1194/07), the US–Israel Binational Science Foundation (Grant 2004-205) and the Research Council of Norway (Grant 177464/V30).

Appendix A. Window functions

For any practical application of the LZE, a window function $g(\boldsymbol{k})$ must be chosen. The formal requirements of the window

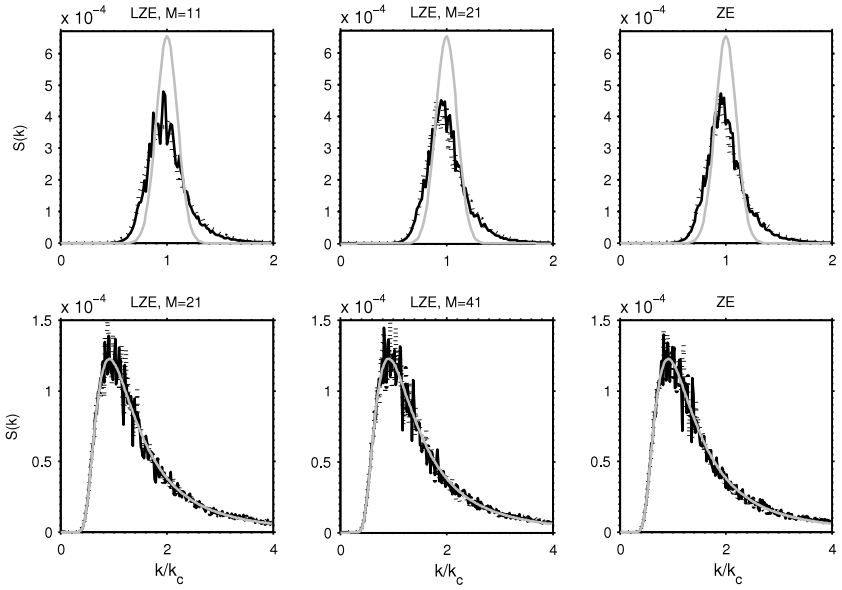

Fig. 7. Evolution of wave spectra obtained from ensemble averaging over 100 runs with different random phases. Upper row: Gaussian initial spectrum; lower row: PM initial spectrum. The solid gray lines show the initial spectra ($t = 0$), solid black lines correspond to $t = 100T_p$, and the dotted lines correspond to $t = 1000T_p$.

functions are that they must be sufficiently localized, i.e. $g(\boldsymbol{k})$ is only nonzero in the vicinity of $\boldsymbol{k} = 0$, and satisfy the normalization criterion (17). In addition, as mentioned in Section 3.3, when it comes to numerical efficiency, it is an advantage if the window functions satisfy some overlapping properties, e.g. that a window only overlaps with its closest neighbors.

When choosing the type of window function, it is also important to have in mind that the purpose of the window functions is to extract information of a function around a certain location. Also, it is clear that every window function applied in wavenumber space corresponds to a certain window in physical space; see e.g. (32). Therefore, it is expected that a window function that is well localized in both physical space and wavenumber space is a good choice.

In the following, we present four possible choices of window function. For convenience, we only consider their one-dimensional versions. The four types of window function, and their correspondences in physical space, are shown in Fig. A.8.

A.1. Square window

A square window with width Δ has the form

$$g(k) = h\left(\frac{k}{\Delta}\right), \qquad G(x) = \frac{\Delta}{\sqrt{2\pi}}\operatorname{sinc}\left(\frac{x\Delta}{2}\right), \tag{A.1}$$

where

$$h(x) = \begin{cases} 1, & |x| < \dfrac{1}{2} \\ 0, & \text{otherwise} \end{cases} \quad \text{and} \quad \operatorname{sinc}(x) = \frac{\sin x}{x}. \tag{A.2}$$

Pros: No overlapping between windows, satisfies the normalization criterion exactly and is easily interpretable in wavenumber space. Cons: Not well localized in physical space.

A.2. Sinc window

$$g(k) = \operatorname{sinc}\left(\frac{\pi k}{\Delta}\right), \qquad G(x) = \frac{\Delta}{\sqrt{2\pi}} h\left(\frac{x\Delta}{2\pi}\right). \tag{A.3}$$

Pros: Satisfies the normalization criterion exactly and is easily interpretable in physical space. Cons: Not well localized in wavenumber space and does not satisfy any overlapping properties.

A.3. Gaussian window

$$\begin{aligned} g(k) &= \frac{\Delta}{\sigma\sqrt{2\pi}} \exp\left(-\frac{k^2}{2\sigma^2}\right), \\ G(x) &= \frac{\Delta}{\sqrt{2\pi}} \exp\left(-\frac{\sigma^2 x^2}{2}\right). \end{aligned} \tag{A.4}$$

Pros: Well localized in both physical and wavenumber space. Cons: Does not satisfy the normalization criterion exactly, but almost for carefully chosen Δ and σ. Does not satisfy any overlapping properties.

A.4. Truncated cos window

$$\begin{aligned} g(k) &= \frac{1}{2}\left[1 + \cos\left(\frac{\pi k}{\Delta}\right)\right] h\left(\frac{k}{2\Delta}\right), \\ G(x) &= \frac{\Delta}{\sqrt{2\pi}} \frac{\operatorname{sinc}(x\Delta)}{1 - \left(\frac{x\Delta}{\pi}\right)^2}. \end{aligned} \tag{A.5}$$

Pros: Well localized in both physical and wavenumber space. In addition, it only overlaps with its closest neighbors and satisfies the normalization criterion exactly.

Appendix B. Reconstruction of η

The solution of Eqs. (32)–(36) gives the variable $B_{m,n} = b_{m,n}\, \mathrm{e}^{\mathrm{i}\omega_{m,n}t}$. From (20), we see that the original Zakharov variable, $\hat{b}(\boldsymbol{k}, t)$, and its inverse Fourier transform, $b(\boldsymbol{x}, t)$, can be expressed as

$$b(\boldsymbol{x}, t) = \sum_{m,n} B_{m,n}(\boldsymbol{x}, t)\mathrm{e}^{\mathrm{i}(\boldsymbol{k}_{m,n}\cdot\boldsymbol{x} - \omega_{m,n}t)}, \tag{B.1}$$

$$\begin{aligned} \hat{b}(\boldsymbol{k}, t) &= \frac{1}{2\pi}\int b(\boldsymbol{x}, t)\mathrm{e}^{-\mathrm{i}\boldsymbol{k}\cdot\boldsymbol{x}}\,\mathrm{d}\boldsymbol{x} \\ &= \frac{1}{2\pi}\int \sum_{m,n} B_{m,n}(\boldsymbol{x}, t)\mathrm{e}^{\mathrm{i}(\boldsymbol{k}_{m,n}\cdot\boldsymbol{x} - \omega_{m,n}t)}\mathrm{e}^{-\mathrm{i}\boldsymbol{k}\cdot\boldsymbol{x}}\,\mathrm{d}\boldsymbol{x} \\ &= \sum_{m,n} \hat{B}_{m,n}(\boldsymbol{k} - \boldsymbol{k}_{m,n}, t)\mathrm{e}^{-\mathrm{i}\omega_{m,n}t}. \end{aligned} \tag{B.2}$$

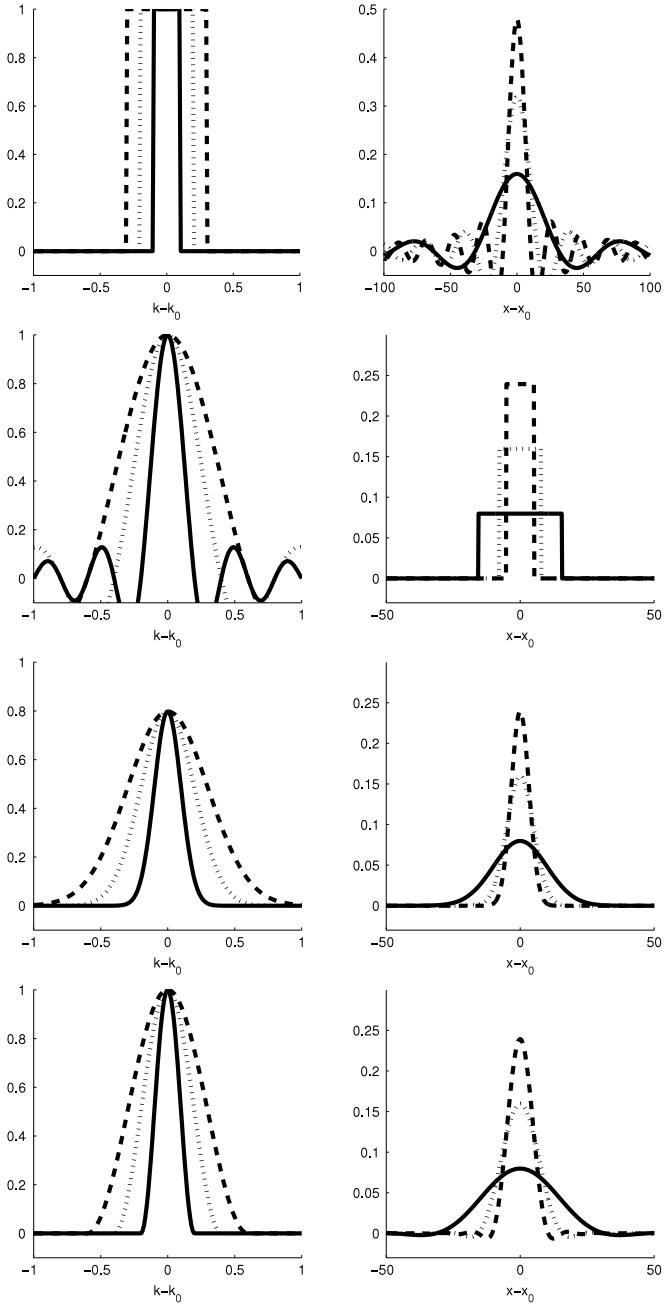

Fig. A.8. Window functions $g(\boldsymbol{k})$ (left) and their correspondences in physical space $G(\boldsymbol{x})$ (right). From top to bottom: square, sinc, Gaussian and truncated cos. $\Delta = 0.2$ (solid line), $\Delta = 0.4$ (dotted line), $\Delta = 0.6$ (dashed line).

The relation between $\hat{b}(\boldsymbol{k}, t)$ and the surface elevation η is given by

$$\eta(\boldsymbol{x}, t) = \frac{1}{2\pi}\int\left(\frac{\omega}{2g}\right)^{1/2}\hat{b}(\boldsymbol{k}, t)\mathrm{e}^{\mathrm{i}\boldsymbol{k}\cdot\boldsymbol{x}}\,\mathrm{d}\boldsymbol{k} + \text{c.c.} \tag{B.3}$$

Inserting (B.2) into (B.3) finally gives

$$\begin{aligned}\eta(\boldsymbol{x}, t) &= \frac{1}{(2\pi)^2}\iint\left(\frac{\omega}{2g}\right)^{1/2}\sum_{m,n}B_{m,n}(\boldsymbol{x}_1, t)\mathrm{e}^{\mathrm{i}(\boldsymbol{k}_{m,n}\cdot\boldsymbol{x}_1-\omega_{m,n}t)}\\ &\quad\times\mathrm{e}^{-\mathrm{i}\boldsymbol{k}\cdot(\boldsymbol{x}_1-\boldsymbol{x})}\,\mathrm{d}\boldsymbol{x}_1\mathrm{d}\boldsymbol{k} + \text{c.c}\\ &= \sum_{m,n}\int\left(\frac{\omega_{m,n}}{2g}\right)^{1/2}B_{m,n}(\boldsymbol{x}_1, t)\\ &\quad\times\mathrm{e}^{\mathrm{i}(\boldsymbol{k}_{m,n}\cdot\boldsymbol{x}_1-\omega_{m,n}t)}\delta(\boldsymbol{x}_1-\boldsymbol{x})\,\mathrm{d}\boldsymbol{x}_1 + \text{c.c}\\ &= \sum_{m,n}\left(\frac{\omega_{m,n}}{2g}\right)^{1/2}B_{m,n}(\boldsymbol{x}, t)\mathrm{e}^{\mathrm{i}(\boldsymbol{k}_{m,n}\cdot\boldsymbol{x}-\omega_{m,n}t)} + \text{c.c.}\end{aligned} \tag{B.4}$$

Note that in our reconstruction we exclude the effect of the higher-order bound modes.

Appendix C. Discretized Zakharov equation

The discretized Zakharov equation obtained in [7] can be derived from the LZE by the following two steps.

(i) Start from (32), and replace $B^*_{m_1,n_1}(\boldsymbol{x}_1)B_{m_2,n_2}(\boldsymbol{x}_1)B_{m_3,n_3}(\boldsymbol{x}_1)$ on the RHS by $B^*_{m_1,n_1}(\boldsymbol{x})B_{m_2,n_2}(\boldsymbol{x})B_{m_3,n_3}(\boldsymbol{x})$, so that they can be taken outside the integral, which then simplifies so that

$$\begin{aligned}&\int\mathrm{e}^{\mathrm{i}(\boldsymbol{k}_{m_3,n_3}+\boldsymbol{k}_{m_2,n_2}-\boldsymbol{k}_{m_1,n_1}-\boldsymbol{k}_{m,n})\cdot\boldsymbol{x}_1}G(\boldsymbol{x}-\boldsymbol{x}_1)\,\mathrm{d}\boldsymbol{x}_1\\ &= \mathrm{e}^{\mathrm{i}(\boldsymbol{k}_{m_3,n_3}+\boldsymbol{k}_{m_2,n_2}-\boldsymbol{k}_{m_1,n_1}-\boldsymbol{k}_{m,n})\cdot\boldsymbol{x}}\\ &\quad\times\int\mathrm{e}^{-\mathrm{i}(\boldsymbol{k}_{m_3,n_3}+\boldsymbol{k}_{m_2,n_2}-\boldsymbol{k}_{m_1,n_1}-\boldsymbol{k}_{m,n})\cdot\boldsymbol{\xi}}G(\boldsymbol{\xi})\,\mathrm{d}\boldsymbol{\xi}\\ &= 2\pi\mathrm{e}^{\mathrm{i}(\boldsymbol{k}_{m_3,n_3}+\boldsymbol{k}_{m_2,n_2}-\boldsymbol{k}_{m_1,n_1}-\boldsymbol{k}_{m,n})\cdot\boldsymbol{x}}\\ &\quad\times g(\boldsymbol{k}_{m_3,n_3}+\boldsymbol{k}_{m_2,n_2}-\boldsymbol{k}_{m_1,n_1}-\boldsymbol{k}_{m,n}).\end{aligned} \tag{C.1}$$

(ii) $g(\boldsymbol{k})$ is taken as (A.1); then $g(\boldsymbol{k}_{m_3,n_3}+\boldsymbol{k}_{m_2,n_2}-\boldsymbol{k}_{m_1,n_1}-\boldsymbol{k}_{m,n})$ can be replaced by $\delta_k(\boldsymbol{k}_{m_3,n_3}+\boldsymbol{k}_{m_2,n_2}-\boldsymbol{k}_{m_1,n_1}-\boldsymbol{k}_{m,n})$, where δ_k denotes the Kronecker δ, and (32) renders

$$\begin{aligned}&\mathrm{i}\left(\frac{\partial B_{m,n}}{\partial t}+\mathbf{c}_{g_{m,n}}\cdot\nabla B_{m,n}\right)+\frac{D^{(xx)}_{m,n}}{2}\frac{\partial^2 B_{m,n}}{\partial x^2}\\ &\quad+D^{(xy)}_{m,n}\frac{\partial^2 B_{m,n}}{\partial x\partial y}+\frac{D^{(yy)}_{m,n}}{2}\frac{\partial^2 B_{m,n}}{\partial y^2}\\ &= 4\pi^2\sum_{m_1,n_1}\sum_{m_2,n_2}\sum_{m_3,n_3}T(\boldsymbol{k}_{m,n},\boldsymbol{k}_{m_1,n_1},\boldsymbol{k}_{m_2,n_2},\boldsymbol{k}_{m_3,n_3})\\ &\quad\times B^*_{m_1,n_1}(\boldsymbol{x})B_{m_2,n_2}(\boldsymbol{x})B_{m_3,n_3}(\boldsymbol{x})\\ &\quad\times\delta_k(\boldsymbol{k}_{m,n}+\boldsymbol{k}_{m_1,n_1}-\boldsymbol{k}_{m_2,n_2}-\boldsymbol{k}_{m_3,n_3})\\ &\quad\times\mathrm{e}^{\mathrm{i}(\omega_{m,n}+\omega_{m_1,n_1}-\omega_{m_2,n_2}-\omega_{m_3,n_3})t}.\end{aligned} \tag{C.2}$$

Given the fact that $B_{m,n}$ here is $(\Delta/2\pi)^2$ times the $B_{m,n}$ of [7], one can see that (C.2) is identical to Eq. (28) in [7], which is the DZE.

Note that step (i) above requires a slow variation of $B_{m,n}$ with $\boldsymbol{x}$. This occurs for spectra which are nonvanishing only in the vicinities of $\boldsymbol{k}_{m,n}$, thus restricting the applicability of the DZE significantly.

Appendix D. Evolution of a Stokes wave

The ZE (2) has the following solution:

$$\hat{b}(\boldsymbol{k}, t) = b_0\mathrm{e}^{-\mathrm{i}\Omega_0 t}\delta(\boldsymbol{k}-\boldsymbol{k}_0), \qquad \Omega_0 = \omega_0 + T_0 b_0^2, \tag{D.1}$$

where $\omega_0 = \omega(\boldsymbol{k}_0)$ and $T_0 = T(\boldsymbol{k}_0, \boldsymbol{k}_0, \boldsymbol{k}_0, \boldsymbol{k}_0)$. For $t = 0$, one has $\hat{b}(\boldsymbol{k}, 0) = b_0\delta(\boldsymbol{k}-\boldsymbol{k}_0)$. Assuming that $\boldsymbol{k}_0$ falls within the bin (M, N), and applying the window (A.1) for simplicity, we find the corresponding initial condition in terms of variables of the LZE:

$$b_{m,n}(\boldsymbol{x}, 0) = \begin{cases}\dfrac{b_0}{2\pi}\mathrm{e}^{\mathrm{i}(\boldsymbol{k}_0-\boldsymbol{k}_{m,n})\cdot\boldsymbol{x}}, & (m,n) = (M,N)\\ 0, & (m,n)\neq(M,N).\end{cases} \tag{D.2}$$

Based on (D.2), we assume a solution to the LZE (6) in the form

$$b_{m,n}(\boldsymbol{x}, 0) = \begin{cases}\dfrac{b_0}{2\pi}\mathrm{e}^{-\mathrm{i}\Omega_{M,N}t}\mathrm{e}^{\mathrm{i}(\boldsymbol{k}_0-\boldsymbol{k}_{M,N})\cdot\boldsymbol{x}}, & (m,n) = (M,N)\\ 0, & (m,n)\neq(M,N).\end{cases} \tag{D.3}$$

Substituting (D.3) into the LZE yields

$$\Omega_{M,N} = \omega_0 + T_{M,N} b_0^2 + O(\Delta^3), \tag{D.4}$$

where $T_{M,N} = T(\boldsymbol{k}_{M,N}, \boldsymbol{k}_{M,N}, \boldsymbol{k}_{M,N}, \boldsymbol{k}_{M,N})$, and where Δ is the width of the bins, i.e. $|\boldsymbol{k}_0 - \boldsymbol{k}_{M,N}| = O(\Delta)$. From (3) and (D.1), one now finds

$$\eta_{\mathrm{ZE}} = \frac{1}{\pi}\left(\frac{\omega_0}{2g}\right)^{1/2} b_0 \cos(\boldsymbol{k}_0 \cdot \boldsymbol{x} - \omega_0 t - T_0 b_0^2 t). \tag{D.5}$$

Correspondingly, (5) together with (D.3) and (D.4) gives

$$\eta_{\mathrm{LZE}} = \frac{1}{\pi}\left(\frac{\omega_{m,n}}{2g}\right)^{1/2} b_0 \cos(\boldsymbol{k}_0 \cdot \boldsymbol{x} - \omega_0 t - T_{M,N} b_0^2 t + O(\Delta^3) t). \tag{D.6}$$

By using (45), one finds that D_{rms} corresponding to the solutions (D.5) and (D.6) is given by

$$D_{\mathrm{rms}} = 1 - \cos([\Omega_0 - \Omega_{M,N}]t) + O(\Delta^2), \tag{D.7}$$

where

$$\Omega_0 - \Omega_{M,N} = T_0 b_0^2 - T_{M,N} b_0^2 + O(\Delta^3) = O(\Delta^3, \epsilon^2 \Delta). \tag{D.8}$$

Consequently, D_{rms} will approach unity on the time scale $t = O(\Delta^{-3}, \epsilon^{-2}\Delta^{-1})$.

References

[1] V.E. Zakharov, Stability of periodic waves of finite amplitude on the surface of a deep fluid, J. Appl. Mech. Tech. Phys. 9 (1968) 190–194.

[2] K. Hasselmann, On the non-linear energy transfer in a gravity-wave spectrum. Part 1. General theory, J. Fluid Mech. 12 (1962) 481–500.

[3] C.C. Mei, M. Stiassnie, D.K.P. Yue, Theory and Applications of Ocean Surface Waves, Part 2: Nonlinear Aspects, in: Advanced Series on Ocean Engineering, vol. 23, World Scientific, 2005.

[4] V.P. Krasitskii, On reduced equations in the Hamiltonian theory of weakly nonlinear surface-waves, J. Fluid Mech. 272 (1994) 1–20.

[5] H.C. Yuen, B.M. Lake, Nonlinear dynamics of deep-water gravity waves, Adv. Appl. Mech. 22 (1982) 67–229.

[6] S.Y. Annenkov, V.I. Shrira, Fast nonlinear evolution in wave turbulence, Phys. Rev. Lett. 102 (2) (2009) 024502. URL: http://dx.doi.org/10.1103/PhysRevLett.102.024502.

[7] J.H. Rasmussen, M. Stiassnie, Discretization of Zakharov's equation, Eur. J. Mech. B Fluids 18 (1999) 353–364.

[8] S.Y. Annenkov, V.I. Shrira, Numerical modelling of water-wave evolution based on the Zakharov equation, J. Fluid Mech. 449 (2001) 341–371.

[9] K.B. Dysthe, Note on a modification to the nonlinear Schrödinger equation for application to deep water waves, Proc. R. Soc. Lond. Ser. A 369 (1736) (1979) 105–114.

[10] K. Trulsen, I. Kliakhandler, K.B. Dysthe, M.G. Velarde, On weakly nonlinear modulation of waves on deep water, Phys. Fluids 12 (10) (2000) 2432–2437.

[11] P.A.E.M. Janssen, Nonlinear four-wave interactions and freak waves, J. Phys. Oceanogr. 33 (4) (2003) 863–884.

[12] D.K.P. Yue, Y. Liu, Direct phase-resolved simulation of large-scale nonlinear ocean wave-field, Tech. Rep., Department of Mechanical Engineering, Massachusetts Institute of Technology, 2005. URL: http://citeseerx.ist.psu.edu/viewdoc/download?doi=10.1.1.129.4256&rep=rep1&type=pdf.